J. Electrochem. Sci. Eng. **14(2)** (2024) 213-229; http://dx.doi.org/10.5599/jese.2139

Open Access : : ISSN 1847-9286
www.jESE-online.org

Original scientific paper

Electrochemical behaviour of thermally treated aluminium 2024 alloy exposed to *B. mojavensis*

Nelson Vejar✉, Joseph Rozas and Roberto Solis

Centro de Investigación y Desarrollo en Ciencias Aeroespaciales, Fuerza Aérea de Chile. Av. José Miguel Carrera 11087, Santiago, Chile

Corresponding author: ✉nelsonvejar.v@gmail.com; Tel.: +56-2-2976 1329

Received: October 17, 2023; Accepted: February 7, 2024; Published: March 13, 2024

Abstract

The copper-rich zone plays a key role in understanding the deterioration process of 2024 aluminium alloy. The intermetallic on the surfaces makes this alloy susceptible to both local corrosion and microbial colonization. The adhesion of bacteria on the surface could deteriorate the metallic substrate in a phenomenon known as microbiologically influenced corrosion (MIC). The triggering mechanism of MIC in 2024-T3 is unclear. An electrochemical study was conducted to determine the influence of the second phase (Al_2Cu) on the corrosion of the 2024-T3 aluminium alloy exposed to bacteria. The 2024-T3 alloy was thermally treated to increase the amount of Al_2Cu by nearly 67 % on the surface. The bacterium under study was collected from the corrosion products of a Chilean Air Force aircraft. The isolated bacterium was identified by 16S RNA sequencing as Bacillus mojavensis (99.99 %). Results obtained by electrochemical impedance spectroscopy showed a decreased impedance of 2024-T3 and an increased impedance of heat-treated, both samples exposed to bacteria. The increased impedance could be associated with the antibacterial effect due to the high ion release of copper on the surface, which can inhibit biofilm formation and biocorrosion.

Keywords
Aluminium alloy; thermal treatment; second phases; biocorrosion; impedance

Introduction

The copper is incorporated in approximately 4-5 % by weight of an aluminium matrix and has allowed the development of 2024 aluminium alloy. The second phase (θ phase) is composed of Al_2CuMg and $Al_2CuMgFe$, improving the mechanical properties of this alloy. Due to this, 2024 aluminium alloy is widely used in the aerospace industry. Despite its good mechanical properties, the θ phases make this material susceptible to corrosion [1,2] and bacterial colonization [3].

The adherence of microorganisms on a metal surface could potentially trigger an increased corrosion rate. The unusual corrosion rate phenomenon of metallic materials is known as microbiologically influenced corrosion (MIC) [4]. Two mechanisms for MIC of 2024 aluminium alloys have been documented: (a) the production of water-soluble organic acids by bacteria and fungi and (b) the formation of differential aeration cells [5]. In recent years, a relation between the enzymatic activity and the adhesion of bacteria on aluminium alloy 2024 and 6063 substrates was found [6]. Paez *et al.* [6] found that *Pseudomonas aeruginosa* increases the concentration of oxygen and hydroxyl ions on the surface due to catalase activity. This phenomenon can promote accelerated corrosion [7]. The accelerated deterioration of 6063 aluminium alloys was attributed to changes in the chemical composition of the surfaces. There is evidence that the chemical characteristics associated with the second phase on the metallic surface can affect bacterial colonization; however, this has not been addressed [8-11]. Rosales and Iannuzi [12] evaluated the thermal treatment 2024-T351 on the MIC phenomenon promoted by the fungus *Hormoconis resinae*. The electrochemical results showed a relation between the thermal treatment and the corrosion. Still, a direct relationship between the concentration and distribution of the second phase and the MIC phenomenon was not described.

A diversity of bacteria and fungi have been isolated from aircraft, and the most common corrosive organism found was the fungus *Hormoconis resinae* [13,14]. In recent years, changes in the chemical composition of fuels and surface treatment to inhibit corrosion have caused a community modification from fungi to bacteria [15]. Bacteria collected by our research group have shown dual behaviour. The corrosion was accelerated [16] and inhibited [17]. Recent research demonstrated increased cathodic current associated with bacterial activity (*Bacillus* species) [18].

This paper aims to determine the effect of the alloying element distribution in the 2024-T3 surface on susceptibility to MIC. Bacteria collected (*Bacillus mojavensis*) from a corrosion product was used. The increased amount of Al_2CuMg precipitates on the surface of the 2024 alloys was obtained using different thermal treatments.

Experimental

Metallic substrate pretreatment

The 2024-T3 sheet (50×50×0.2 mm) was provided by the National Aeronautical Company of Chile (Spanish abbreviation, ENAER). The chemical composition of this alloy was (in wt.%): 0.087 Si, 0.151 Fe, 4.940 Cu, 0.780 Mn, 1.480 Mg, 0.006 Cr, 0.009 Ni, 0.029 Zn, 0.039 Ti, 0.010 Sn, and Al balanced. The metallic surfaces were mechanically polished using #800, # 1000, and #1500 SiC paper. Then, the samples were washed using an ultrasonic ethanol bath for 5 min to remove the solid particles from the mechanical polishing. All samples were sterilized by UV light for 12 min [16] before the microbiological procedure.

Isolation and identification of bacterial strains

The bacterial strain was collected from the corrosion products on an aircraft surface exposed to the coastal environment (north of Chile). The biological sample was maintained in a sterilized flask (1.5 mL) and transported to the laboratory. The bacterium was inoculated (0.1:10) aseptically in a nutritive broth (Luria Bertani, LB). The composition of the culture broth in water (ultra-pure, Milli-Q quality, 18.2 MΩ cm^{-1}) consisted of 10 g L^{-1} tryptone, 5 g L^{-1} yeast extract and 10 g L^{-1} NaCl. The flask was placed in an incubator (Biobase) at 30 °C for 16 h and serial dilutions of the solution (10^{-1} to 10^{-6}) were prepared using sterile phosphate buffer (pH 7.0). Next, 100 µL of each dilution was spread on LB medium plates and incubated at 30 °C for 24 h [18]. The strain was stored at -18 °C to ensure the bacterial material purity. The microorganisms were identified by sequencing the 16 s rRNA gene. The sequences obtained were assembled, analysed, and edited manually using the ChromasPro software (Technelysium Pty Ltd.) for a final sequence extension of ~450 bp. The strain was taxonomically classified using the Naïve Bayesian rRNA classifier function from the RDP-Ribosome Database Project [19]. A neighbouring junction tree based on 16S rRNA gene sequences available in databases was generated using the ‘‘NCBI Blast” to determine the phylogenetic distance between isolated bacteria. A 97-100 % match for the GenBank dataset genetically unknown material was considered an acceptable identification [20]. The morphology of the bacteria was characterized by an optical microscope (Bio2T-PLLedpplan, Bel Engineering).

Thermal treatments

The thermal treatments were carried out in a furnace (Barnstead Thermolyne 600,0), and the subsequent stages applied to 2024 aluminium alloy are described below.

a. ThT 01: First, the alloys were treated by 2 h at 510 ± 6 °C (liquid phase/LP). Then, the specimens were removed from the furnace and cooled in a desiccator to 21 °C.
b. ThT 02: The metallic samples were treated by 2 h at 510 ± 6 °C. Then, the samples were cooled inside the furnace to 20 °C, the temperature drop rate was 4 °C min^{-1}
c. ThT 03: The samples were treated by 2 h at 510 ± 6 °C. Then, the specimens were cooled inside the oven in two stages, 410 °C for 45 min and 310 °C for 45 min. Finally, the specimen samples were removed from the furnace and cooled in a desiccator to 21 °C.
d. ThT 04: First, the alloys were treated during 2 h at 510 ± 6 °C. Then, the samples were cooled inside the furnace in three stages: 410 °C for 45 min, 310 °C for 45 min, and finally, cooled to 20 °C, the temperature drop rate was 4 °C min^{-1}.
e. ThT 05: First, the samples were heated from 20 to 510 ± 6 °C; the temperature rise rate was 4 °C min^{-1}. Then, alloys were heated for 2 h at 510 ± 6 °C. Finally, the specimens were removed from the furnace and cooled in a desiccator to 21 °C.
f. ThT 06: First, the alloys were heated inside the furnace from 20 to 510 ± 6 °C, the temperature rise rate was 4 °C min^{-1}. Then, alloys were heated for 2 h at 510 ± 6 °C. Finally, the samples were cooled inside the furnace to 20 °C. The temperature drop rate was 4 °C min^{-1}.

Electrolyte-culture medium

The metallic substrates were exposed to two different systems: a sterile electrolyte-culture (EC) medium (pH 4.8) and an inoculated EC medium with collected bacteria. The EC medium contains (in g L^{-1}): 0.22 $(NH_4)_2SO_4$, 18.70 $NaSO_4$, 0.58 NaCl, 1.20 KH_2PO_4, 0.23 $MgSO_4\times7H_2O$, 0.25 $CaCl_2\times2H_2O$, 0.024 g yeast extract and 0.024 g tryptone [18].

Previously to the inoculation of microorganisms (10 vol.%), the bacteria were grown in LB broth at 27 °C overnight and pelleted. The inoculated EC medium has 10^7 CFU mL^{-1}, which was determined by monitoring the optic density (UV-Vis at 620 nm) and using the McFarland method. Every 4 days, 70 % of the medium was removed and replaced with fresh sterile EC, and the bacteria was inoculated to maintain the density near a steady state during the experiment. The pH values were monitored by a pH meter (Hanna- EDGE).

Electrochemical impedance spectroscopy

Electrochemical measurements were performed with a three-electrode cell configuration. A pure graphite rod (diameter, 6 mm) and a saturated calomel electrode (SCE) were used as a counter and reference electrode, respectively. A delimited area (12.5 cm^2) of the working electrode (2024-T3 sheet) placed at the bottom of the electrochemical cell was sealed with an O-ring. The electrolyte consisted of a sterilized and inoculated EC medium. The electrochemical measurements were carried out using a potentiostat (VSP, Bio-Logic, USA) after exposing the metallic sample to sterile and inoculated EC for 3, 7, 14, and 21 days at 27 °C. The open circuit potential (OCP) was measured until its stabilization before each electrochemical measurement. The EIS data were performed at OCP, from 100 kHz to 10 mHz with 7 points per decade and using 10 mV peak-to-peak sinusoidal potential. The Kramers-Krönig relation was utilized to adjust the frequency range analysed, and impedance data were fitted using a home-developed software called SIMAD (LISE UPR 15 CNRS, France). The equivalent circuits were proposed by EIS data analysis using a DRTtools (Distribution of Relaxation Times tools) of MATLAB software [21]. All measurements were carried out in triplicate to ensure reproducibility.

Distribution and morphology characterization

The metallic samples dimensioned in 1×2 cm were mounted in Bakelite resin using a compression mounting system (Buehler SimpliMet 2), then were cloth polished (Struers LaboPol-5 / 0.03 mm alumina suspension) and washed in acetone and deionized water. The images were evaluated using software (Imagen-Pro Plus) to determine the area of the intermetallic zone.

The morphologies of the metallic substrates (2024-T3 and thermally treated) were evaluated with scanning electron microscopy (SEM), TESCAN S8000. An accelerating voltage of 15 kV was used for the local surface analyses.

Results and discussion

Collection, isolation, and identification of bacteria

The biological sample was collected from the inside of an aircraft wing, which had been exposed to motor oil (Figure 1a). The bacteria were isolated through several serial dilutions and plating rounds of LB solution (Figure 1c) and observed by a microscope that revealed a rod-like shape, the size was close to 1-1.3 µm (Figure 1d).

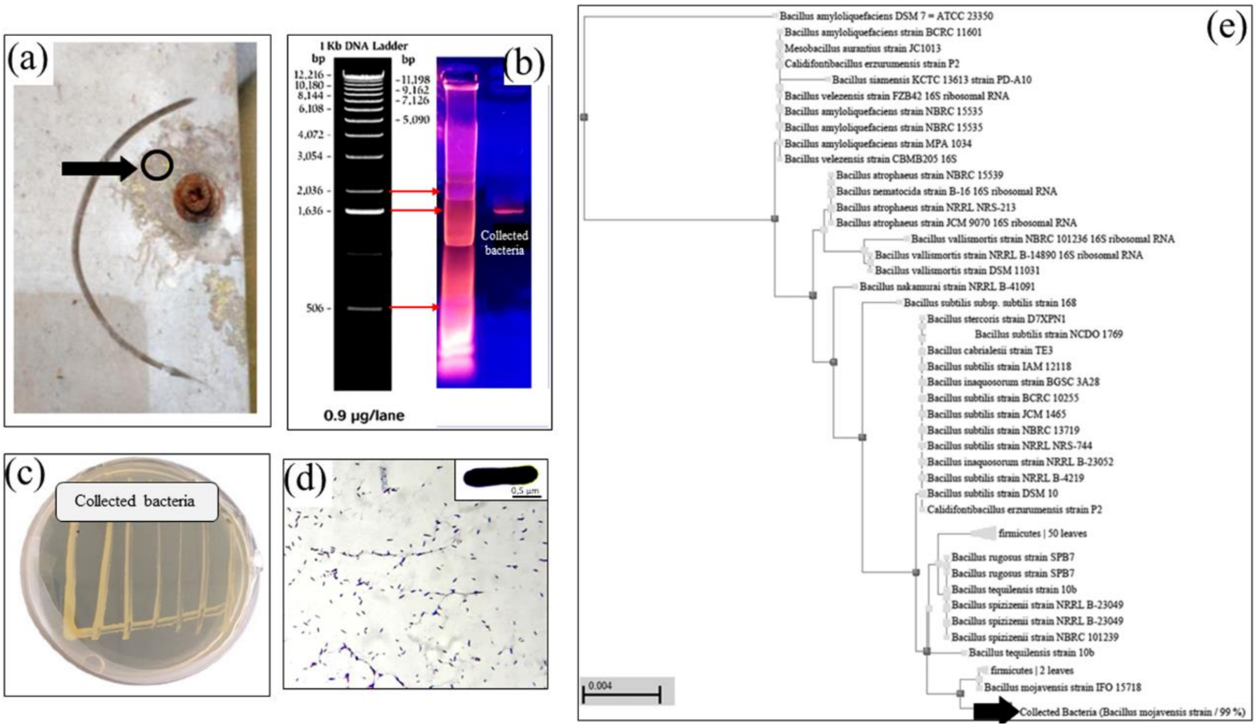

Figure 1. *Isolation and identification of bacteria: (a) collection site, (b) fluorescent images of electrophoresis, (c) growth bacteria on LB-dish, (d) optic image, and (e) phylogenetic tree of members of the genus Bacillus, based on 16S rRNA gene sequences*

To ensure a good identification, after performing the PCR (polymerase chain reaction), an agarose gel electrophoresis was performed (Figure 1b), which indicates the base pairs are in the range of 1400 to 1600 bp. Using the Basic Local Alignment Search Tool (BLAST) database, the 16S rDNA sequence analysis revealed a close relation of collected bacteria with the *Bacillus mojavensis* strain (99.99 %) [22]. Figure 1e shows the neighbour-joining tree based on 16S rRNA gene sequences, showing the phylogenetic relationships.

Thermal treatments

The thermal treatment of 2024-T3 samples included homogenization, quenching, cold work, and natural aging. The main alloying elements are copper and magnesium, contributing to strength through aging phenomena [23]. It is possible to obtain a coherent precipitate (intermetallic compound) with the matrix, small, spherical, and well distributed, which mechanically increases the resistance of the alloy in a homogeneous way.

To evaluate the influence of the intermetallic compound on the susceptibility to corrosion and microbial colonization, this phase was highly concentrated, that is, a thermal treatment that reverses the morphology of the precipitation of T3 treatment. No regulated and established thermal treatments are normally used for this, so in the present study, a series of different thermal treatments that largely concentrated the intermetallic phase of the alloy were carried out. Six unconventional treatments focused on the greatest quantities of the intermetallic phase, with *ThT 05* being the one with the greatest amounts of this phase.

At temperatures below the solvus, this alloy equilibrium state consists of two solid phases: solid solution α, plus an intermetallic compound phase θ (Al_2Cu). When such an alloy is converted to a completely solid solution by keeping it above the solvus temperature, and then the temperature decreases below the solvus, the solid solution becomes supersaturated, and the alloy seeks the two-phase equilibrium condition; the second phase tends to form by precipitation in the solid state [24]. According to the above, with the ThT 05 treatment, the diffusion and concentration of the intermetallic compound in different alloy sectors (such as grain boundaries) were promoted due to the times and cooling used, achieving efficient inversion of treatment of T3.

The thermal treatments performed on aluminium alloys were characterized by optical microscopy. The images obtained and a scheme of the methodology applied are presented in Figure 2.

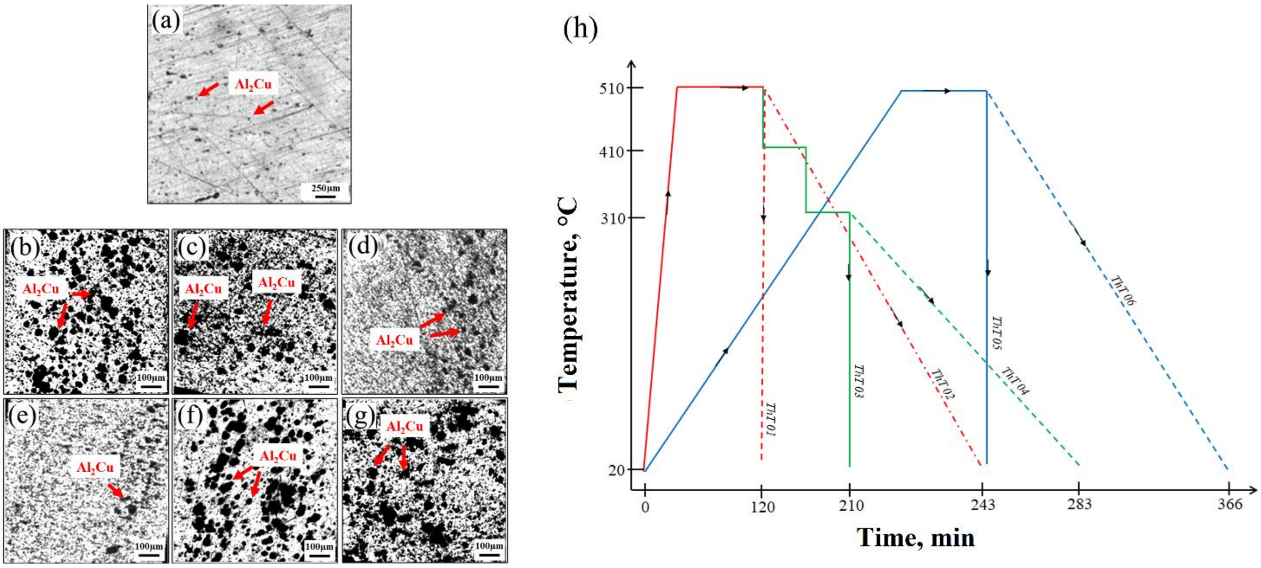

Figure 2. *Optic microscopy images of alloy 2024: (a) 2024-T3, and thermally treated (b) ThT 01, (c) ThT 02, (d) ThT 03, (e) ThT 04, (f) ThT 05, and (g) ThT 06. (h) Scheme of thermal treatment methodology*

Subsequently, the images were evaluated using software to determine the area of the intermetallic precipitates. The results were expressed as a percentage and presented in Table 1.

The percentage of the coverage area of precipitates (second phase) after the heat treatment of 2024 aluminium samples (Table 1) shows increased second phases in the ThT 05 sample compared to the other treatments, with a percentage of ~67.7 %. The heated samples under a temperature rise rate of 4 °C/min (Figure 2h) allowed a high intermetallic concentration with the size of the second phase of ~25 µm (Figure 2g, ThT 05) compared with 5 µm of 2024-T3 (not shown). These results allow us to evaluate the effect of intermetallic of ThT 05 with 2024-T3 exposed to bacteria.

Table 1. *Coverage area of Al_2Cu on the metallic surface of aluminium alloy 2024*

Thermal treatment	2024-T3	ThT 01	ThT 02	ThT 03	ThT 04	ThT 05	ThT 06
Coverage area, %	1.3 ± 0.10	47.2 ± 0.20	38.9 ± 0.15	33.7 ± 0.25	35.9 ± 0.17	67.7 ± 0.13	44.3 ± 0.15

Electrochemical impedance spectroscopy and graphical method analysis

Figures 3 and 4 show the 2024-T3 and ThT 05 EIS plots, respectively. The metallic samples were exposed to a sterile and inoculated medium with *B. mojavensis*.

To facilitate obtaining the EIS parameters through the graphical method, the data were corrected for the electrolyte resistance values, which are reflected in the Nyquist plots with graphs plotted from the origin and observing a constant slope from high to medium frequencies in impedance modulus *vs.* frequency graphs.

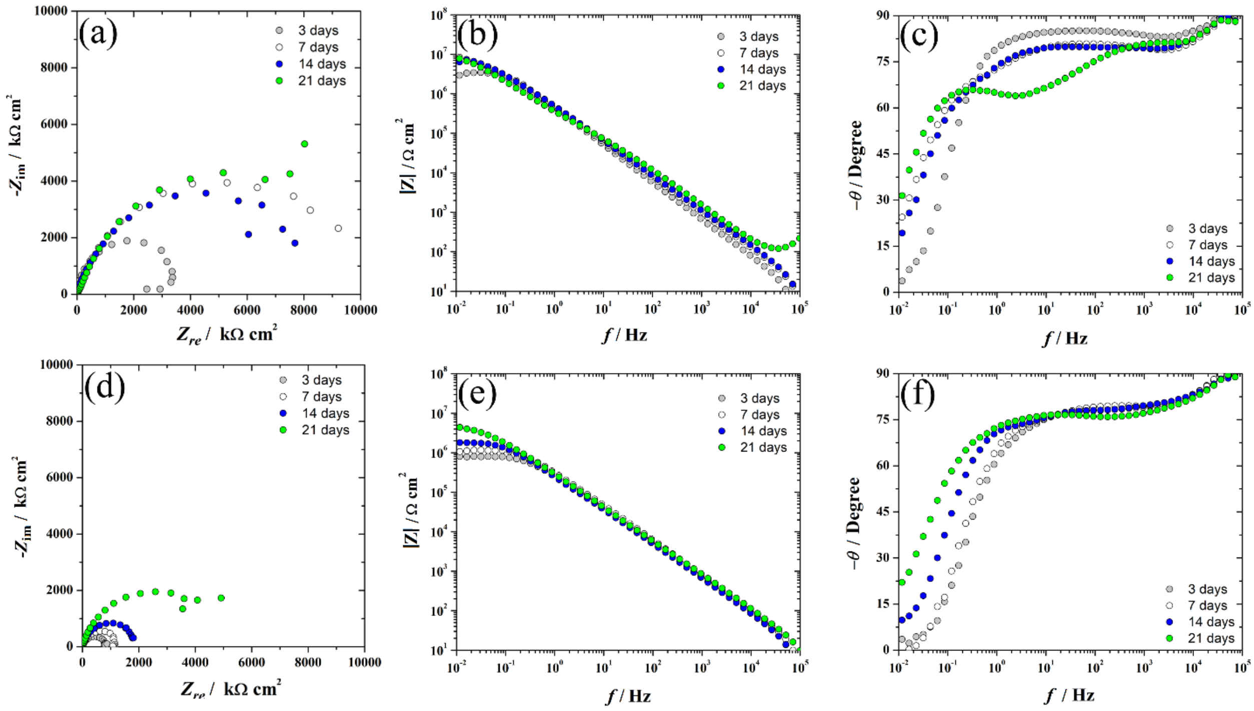

Figure 3. *EIS plots of 2024-T3 exposed to (a, b and c) sterile and (d, e and f) inoculated EC medium with Bacillus mojavensis*

The CPE (constant-phase element) parameters of *Q* and *α* were obtained using the graphical method, as shown in Figure 5, and corresponding data are presented in Table 2. The polarization resistance (R_p) and open circuit potential (OCP) were resumed in Figure 6.

The impedance of a CPE is given by Eq (1):

$$Z_{\mathrm{CPE}}(\omega)=\frac{1}{(j\omega)^{\alpha}Q} \tag{1}$$

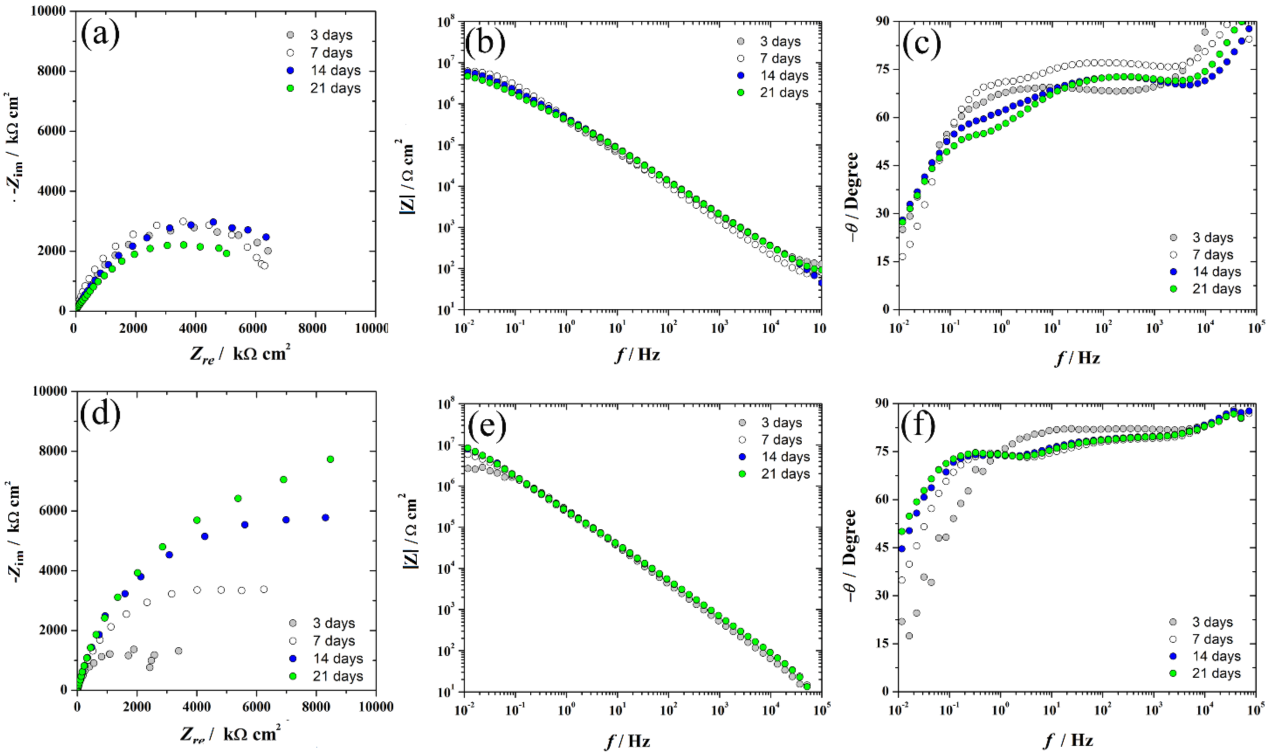

Figure 4. *EIS plots of ThT 05 exposed to (a, b and c) sterile and (d, e and f) inoculated EC medium with Bacillus mojavensis*

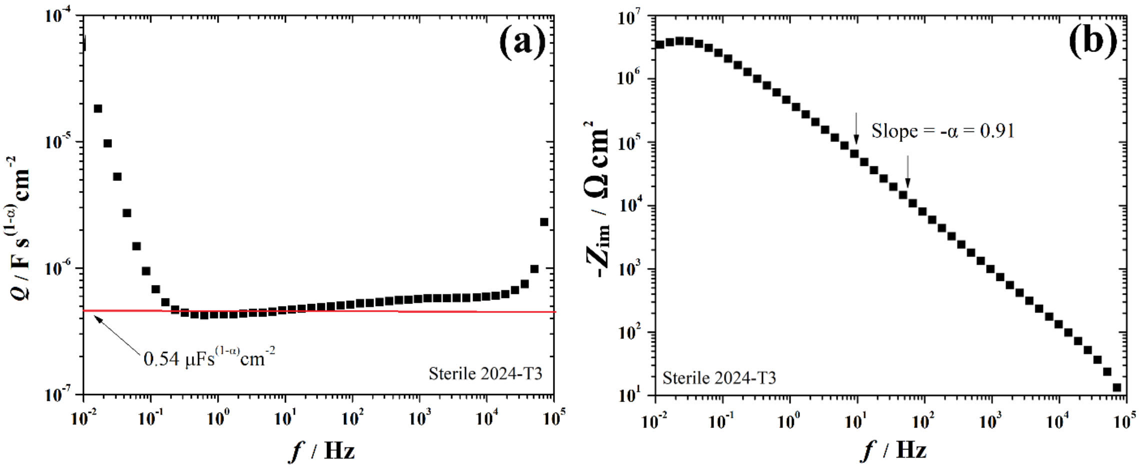

***Figure 5**. Graphical analysis of the impedance calculated for EC described by a CPE: (a) variation of the parameter Q of the CPE and (b) variation of the imaginary impedance part as a function of the frequency*

The α parameter (Eq. 1) is dimensionless and varies between 0 and 1. When $\alpha = 1$, it corresponds to a pure capacitor system. Note that the values can also be determined by a graphical method using log Z_{im} *vs*. log frequency plots, particularly from the negative slope in the frequency range where the CPE appears, as shown in Figure 5(b). In addition, Q is expressed in F s$^{(\alpha-1)}$ cm^{-2}, which can be calculated using the values determined graphically according to Eq. (2):

$$Q = \frac{-1}{Z_{\mathrm{i}}\omega_{\alpha}}\sin\frac{\alpha\pi}{2} \tag{2}$$

Figure 5(a) shows the variation of Q parameter as a function of the frequency for the 2024-T3 sample after exposure to the solution at 21 °C, revealing that the effective Q values are determined from the plateau at the middle-frequency range [25]. The Q values were determined at the medium frequency range, corresponding to the oxide film element. The Q values represent the heterogeneity of the surfaces and are useful when compared with a control system.

On the other hand, the electrolyte resistance (R_e) values were obtained from Nyquist plots at high frequency, from $Z_\mathrm{real,}$ when $Z_\mathrm{im} = 0$. The R_e gives information about the electrolyte near the metallic surface, and chemical reactions on the surface strongly influence this parameter. The low-frequency graphical method and fitting data were applied to determine the impedance values of the oxide film.

Table 2. *EIS parameters of samples 2024-T3 and ThT 05 after 3, 7, 14 and 21 days of exposure to sterile and inoculated EC solution at 21 °C. Values estimated by graphical method*

Sample	Parameter	Exposure time, day			
		3	7	14	21
Sterile 2024-T3	R_e / Ω cm^2	820.3 ± 10.4	905.4 ± 15.4	1084.6± 8.5	723.3± 7.8
	R / kΩ cm^2	2901.2	8346.6	6406.9	7728.3
	Q / μF s$^{(\alpha-1)}$ cm^{-2}	0.47	0.39	0.41	0.35
	α	0.91	0.88	0.89	0.73
Inoculated 2024-T3	R_e / Ω cm^2	1025 ± 17.1	999.3 ± 27.3	722.3 ± 11.1	913.8 ± 8.9
	R / kΩ cm^2	883.2	1040.4	1691.5	5188.9
	Q / μF s$^{(1-\alpha)}$ cm^{-2}	0.61	0.57	0.63	0.55
	α	0.84	0.84	0.85	0.85
Sterile ThT 05	R_e / Ω cm^2	1275 ± 10.1	1400 ± 13.3	1206 ± 15.9	1178 ± 20.2
	R / kΩ cm^2	6419.5	6378.8	6313.4	5212.8
	Q / μF s$^{(1-\alpha)}$ cm^{-2}	0.35	0.33	0.28	0.27
	α	0.76	0.85	0.80	0.80
Inoculated ThT 05	R_e / Ω cm^2	638.8 ± 13.5	805 ± 19.6	941.3 ± 21.2	852.3 ± 10.8
	R / kΩ cm^2	3674.3	6467.3	9089.4	9861.2
	Q / μF s$^{(1-\alpha)}$ cm^{-2}	0.71	0.78	0.61	0.66
	α	0.91	0.84	0.84	0.84

From the EIS results, the specimens of 2024-T3 exposed to sterile EC medium (Figure 3a-c) showed an increased impedance related to exposure time, while the metallic samples exposed to inoculated EC with *B. mojavensis* (Figure 3d-f) showed a decreased impedance for all times compared with the samples exposed to sterile EC medium (Figure 3a-c). General impedance analysis showed an increased impedance with the exposure time for all samples exposed to sterile and inoculated media.

The decreased impedance of alloys exposed to inoculated EC could be attributed to the metabolic activity of bacteria. The effects of corrosion due to the *Bacillus genus* have been reported for 7075 [26] and 2024 alloys [18]. The accelerated corrosion was associated with changes in local pH due to the catalase enzyme, which affects the cathodic reaction. For our studies, the local pH was not determined because the EIS results did not suggest a pH change to an alkaline direction. Still, another process could be associated with organic acid production, which can dissolve the aluminium matrix [27].

The presence of bacteria on ThT 05 surfaces (Figure 4c-f) showed an increased impedance value at all exposure times compared with the samples exposed to a sterile EC medium (Figure 4a-c). Moreover, the impedance increased with the exposure time of all samples in sterile and inoculated medium.

The Q values obtained from EIS (Table 2) of metallic samples exposed to *B. mojavensis* showed an increased value due to the presence of microorganisms in comparison with samples exposed to sterile media. The alfa values of the CPE obtained are very similar, indicating that the system has a deviation of the ideality of a capacitor. Values of 0.61-0.91 were found, and decreased values were shown for ThT 05 exposed to bacteria, due to a diffusion phenomenon that may associated with organic materials from dead cells adsorbed on the metallic surfaces.

R_e values are generally stable for each system in time, and the change of R_e with the exposition time is similar. The values of 2024-T3 exposed to sterile media and bacteria are almost the same due to the same corrosion product. This means the mechanism is very similar, suggesting that bacteria only influence kinetic reactions. A decreased R_e value of ThT 05 exposed to *B. mojavensis* was observed, probably due to the dead cell and lysis, which can release active compounds and molecules that could react with the metallic surface, changing the R_e.

OCP results (Figure 6a) showed a displacement to positive values for 2024-T3 and ThT 05 exposed to bacteria, in contrast to samples exposed to sterile EC. However, these changes could have a different cause because bacteria increase corrosion of 2024-T3 and inhibit corrosion of ThT 05.

The change towards positive values is associated with microorganisms on the metal surface. Results obtained by Starosvetsky *et al.* [28] showed that bacteria adhered to a steel surface shift the potential in a positive direction by approximately 100 mV. The results were attributed to the formation of corrosion products. Little and Lee [3] indicated that a shift in positive values of OCP could reflect bacterial growth and a change in the local environment induced by the metabolic activities of the bacteria, resulting in metal corrosion.

On the other hand, the decreased OCP values of ThT 05 could be attributed to the increased second phases on ThT 05 (copper-rich). These cathodic sites could shift their potential to the cathodic region.

Figure 6b shows the resistance values of the 2024-T3 and ThT 05 samples exposed to sterile and inoculated EC with B. mojavensis. The resistance values were obtained from the Bode plot (modulus) at 20 mHz. The values were compared with both, those obtained with the Nyquist plot when Z_{im} = 0 (low frequency) and the curve fitting method. A marked decrease in values can be observed for 2024--T3 exposed to bacteria compared to those exposed to a sterile medium. The decreased resistance may be due to the activity of bacteria, which accelerate the degradation of the metallic substrate. On the other hand, in the case of ThT 05, an increase in corrosion resistance values was observed, possibly due to the antibacterial properties of copper [29]. An accumulation of dead cells on the metallic surface was speculated, which could show a protective effect of bacteria over the corrosion process.

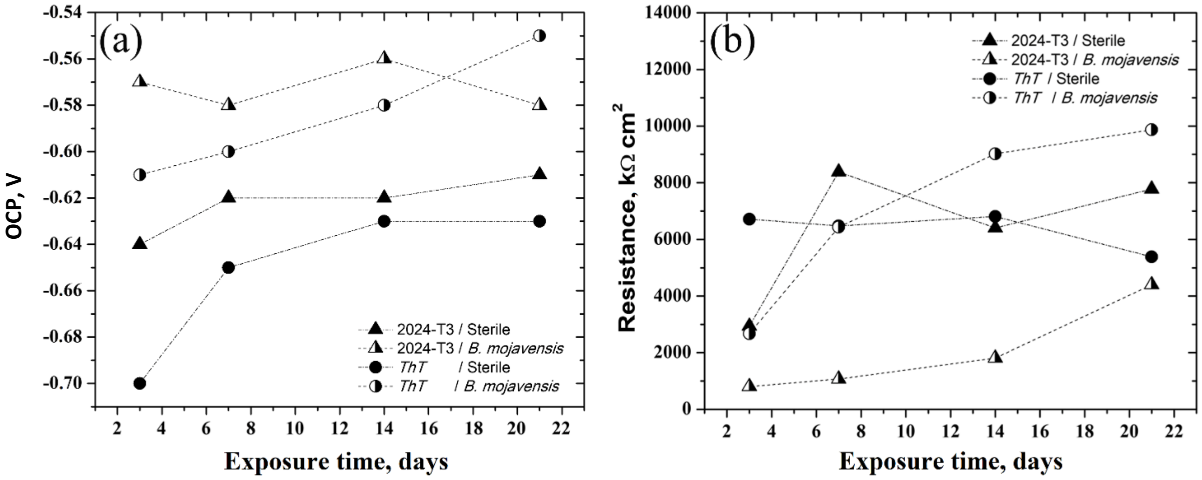

Figure 6. *Open circuit potential (a) and oxide film resistance (b) of 2024-T3 and ThT 05 exposed to sterile and inoculated EC media*

Equivalent circuit and fitting of experimental data

In order to obtain an equivalent circuit, the data were fitted with different software. Due to the change observed on the metallic substrate, a specific difficulty of EIS experiments is the stability during a measurement. Testing the integrity of measured data is an important analysis issue. The Kramers-Kronig relation was used to determine the integrity, this was carried out using an evaluation between the real and imaginary part of the electrical impedance defined by plotting the measured data Z' and Z'' against those calculated from the integrals [30].

A more detailed analysis may be obtained by an examination of residual errors shown in Figure 7, indicating that the measurement model provided a good fit to the data.

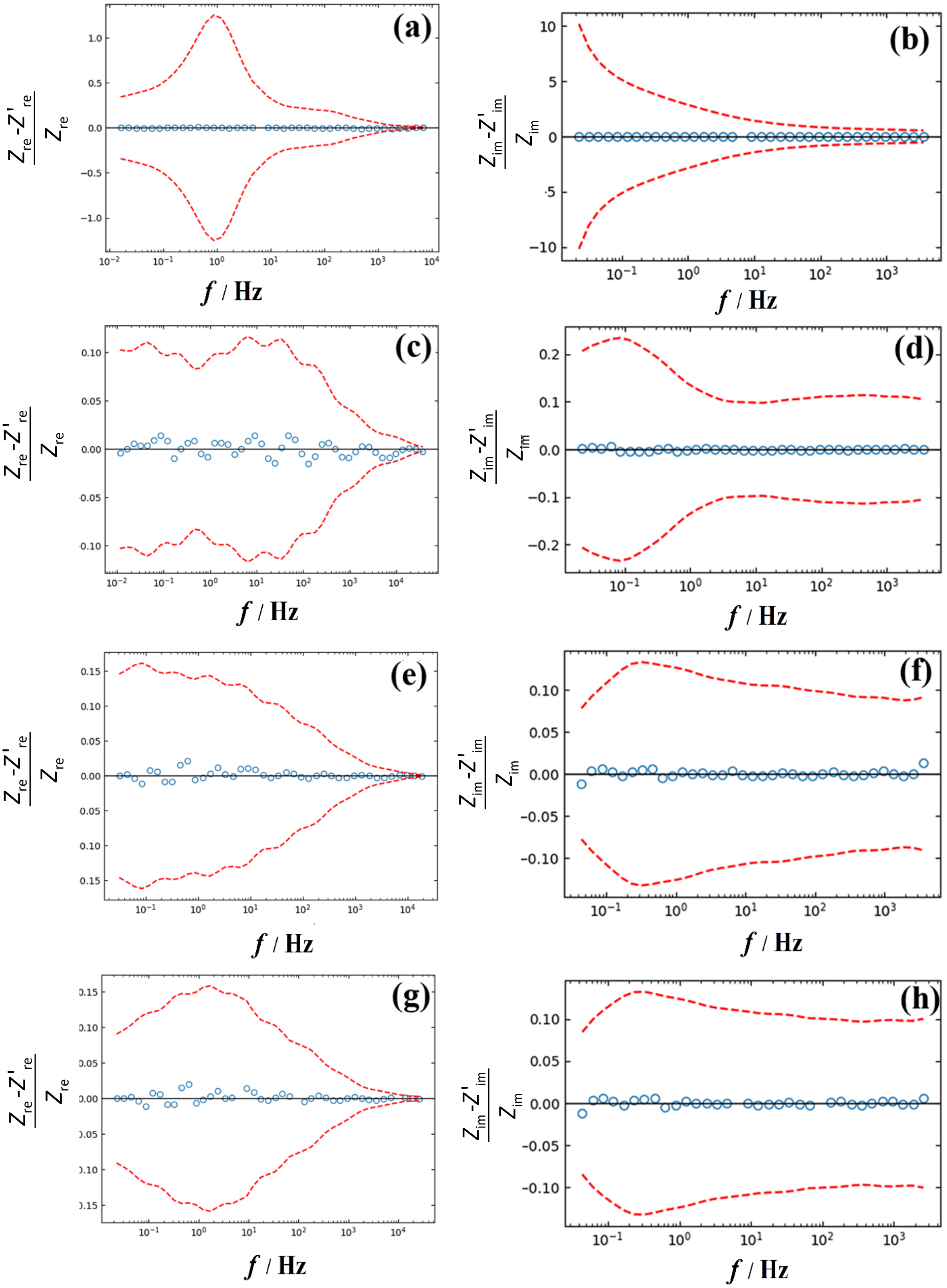

Figure 7*. Normalized residual errors resulting from a measurement model fit (Z′) and of the measurement of metallic samples (Z) at 21 days of exposition to the sterile electrolyte of (a,b) 2024-T3 and (c,d) ThT 05, and exposed to inoculated media (e,f) 2024-T3 and (d) ThT 05. (a, c, e and g) real part and (b, d, f and h) imaginary part*

Figure 7 shows the residual errors (circles) of real and imaginary parts of the Nyquist plot. Red dashed lines represent 95.4 % confidence intervals for the model. The residual errors fall within the 95.4 % confidence interval for the model, and thus, the data may be considered consistent with the Kramers-Kronig relations. This method allows us to have data within the reliable frequency range, which will later be used for a second approach using Zview software and DRTtool.

The main goal of the DRT is to identify the characteristic distribution of typical EIS timescales. The experimental data measured at given frequencies are “fitted” against a model (Z_{DRT}) obtained from the following expression.

$$Z_{\mathrm{DRT}} = R_{\infty} + \int_{-\infty}^{\infty} \frac{\gamma(\tau)}{1+j\omega\tau}\mathrm{d}\tau \tag{3}$$

where ω is the angular frequency, R_{∞} is the ohmic resistance, j is the imaginary part, and $\gamma(\tau)$ is the desired DRT function. The “model” is commonly approximated using Voigt circuits. This approximation can be understood by writing $\gamma(\tau)$ as a sum of Dirac distributions $\delta(\tau)$ centered at times τ_1, τ_2 , … , $\tau_{1\mathrm{M}}$, *i.e*.

$$\gamma(\tau) = \sum_{\mathrm{m}=1}^{\mathrm{M}} x_{\mathrm{m}} \delta(\tau - \tau_{\mathrm{m}}) \tag{4}$$

where x_{m} are unknown parameters to be estimated by fitting. The results are shown in Figure 8 (a-b), where γ(τ) is the distribution function of relaxation times.

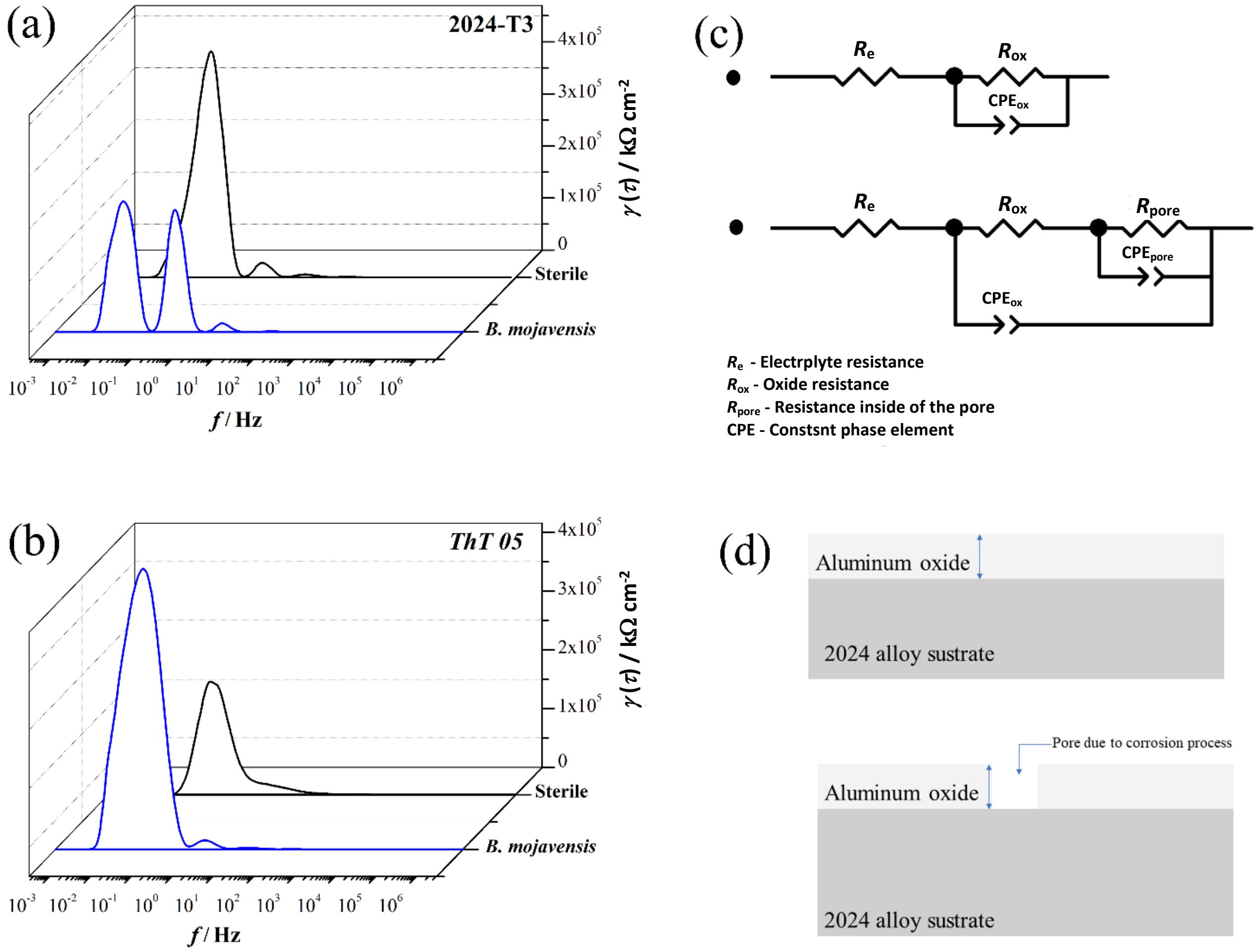

Figure 8. *DRT-function (γ(τ)) plots of (a) 2024-T3 and (b) ThT 05 exposed to inoculated media. (c) proposed equivalent circuits and (d) scheme of oxide film*

The analysis of the distribution of relaxation times, in general, showed single-time constants associated with the aluminium oxide and pores due to the corrosion process. For 2024-T3 exposed to bacteria, an extra time constant is obtained, which could be associated with biofilms adhered to metallic surfaces [29]. The proposed equivalent circuit considering time constants is shown in Figure 8c. A representative scheme of surface conditions is shown in Figure 8d.

To validate the equivalent circuit, these were considered to fit data using Zview. The fitted impedance data of 2024-T3 and ThT 05 exposed to sterile and inoculated media with *B. mojavensis* are presented in Figure 9, where measured data are shown by circles and fitted data by lines. The results showed a good correlation with the circuit selected. The results showed a CPE (constant phase element) behavior, which could be related to the heterogeneous surface.

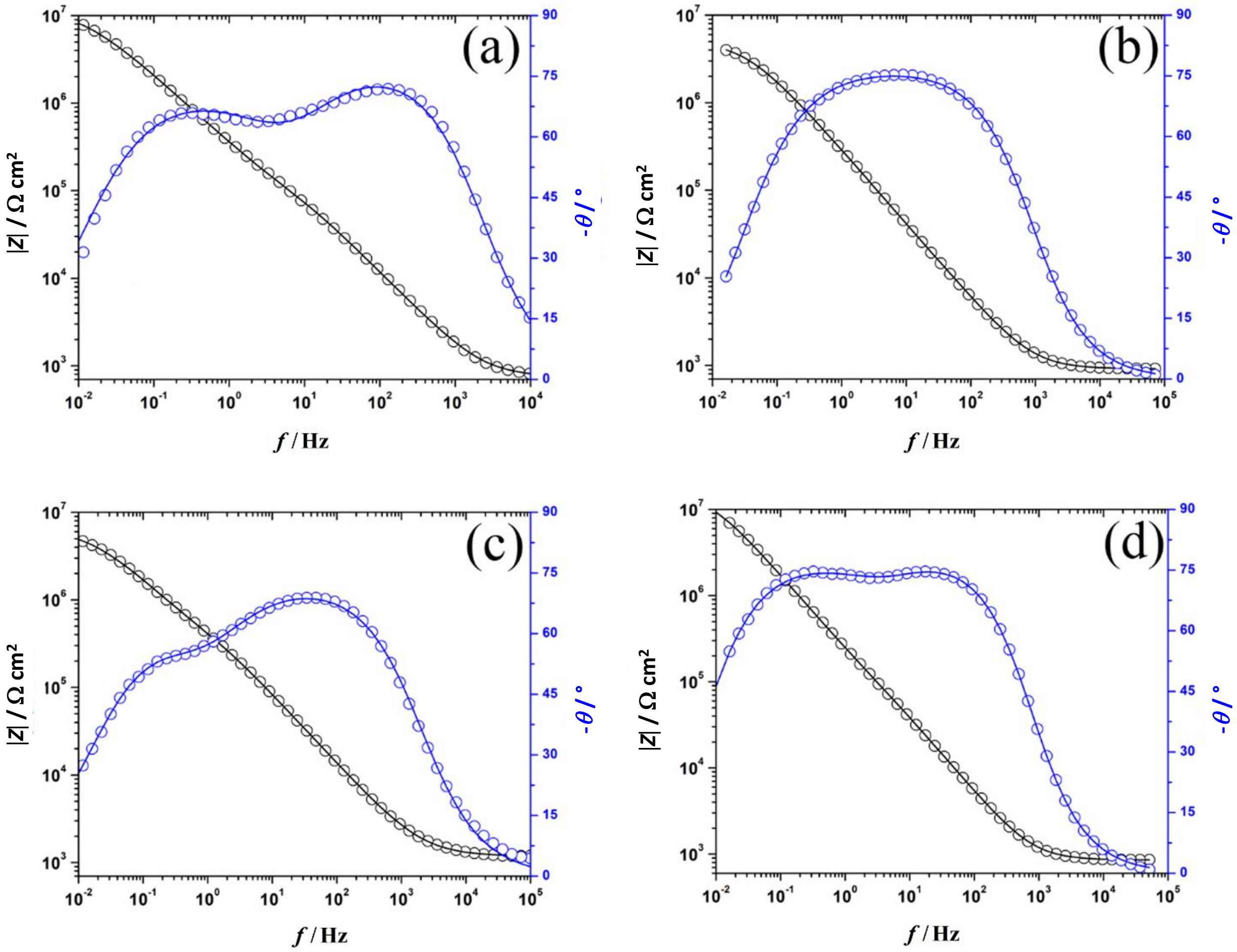

***Figure 9**. Fitted Bode impedance data of metallic samples at 21 days of exposition. Sterile electrolyte (a) 2024-T3 and (b) ThT 05, and inoculated media (c) 2024-T3 and (d) ThT 05. The circles represent the experimental data and lines the fitted data*

Resistance data analysis

Resistance values were obtained at low frequency using log modulus *Z vs*. log *f* but these values could also be obtained by Nyquist plots, as shown in Figure 10.

An alternative way to obtain the resistance values could be using SIMAD with a proposed circuit and the Kramers-Kronig correlation (k-kC). However, due to the discarded values of data due to k-kC, not all results of resistance were obtained. The values considering different methods are shown in Table 3

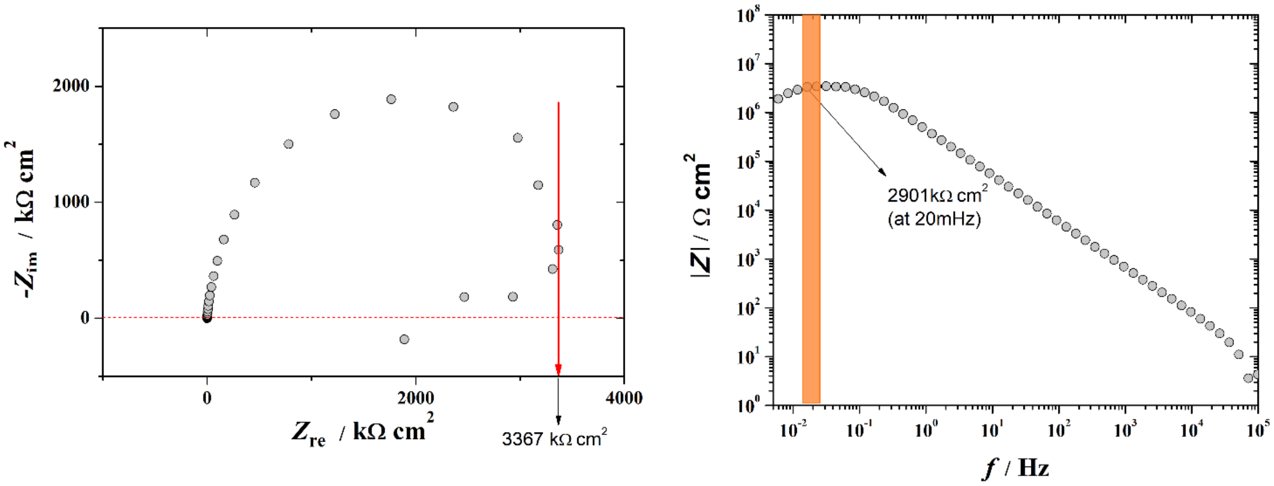

***Figure 10**. Determination of resistance values by graphical analysis from (a) Nyquist and (b) Bode plot of alloy exposure 3 days to sterile electrolyte*

***Table 3.** Comparison of resistance values obtained by different methods*

Samples	Time, day	Graphical method		Software method	
		Modulus graph	Nyquist graph	SIMAD	Kramers-Kronig
		R / kΩ cm^2 (at 20 mHz)	*R* / kΩ cm^2* (HF at Z_{im}=0)	Resistance, kΩ cm^2	
Sterile 2024	3	2901	3367	3800	Not applied
	7	8346	9238	9600	Not applied
	14	6406	7702	8400	Not applied
	21	7728	8002	13000	9600
Sterile ThT 05	3	6419	6425	8400	Not applied
	7	6378	6333	15000	10000
	14	6313	6310	9200	Not applied
	21	5212	5001	6800	Not applied
Inoculated 2024	3	883	93	800	Not applied
	7	1040	30	1300	Not applied
	14	1691	334	1900	Not applied
	21	5188	1701	4900	Not applied
Inoculated ThT 05	3	3674	1388	2800	Not applied
	7	6467	3375	8800	Not applied
	14	9089	5853	15000	1800
	21	9861	7754	18000	4800

*R_{HF}- Resistance obtained at high frequency

Table 3 shows that the resistance values vary from one method to another, the method where it is extrapolated to the Z_{real} axis contains a greater error because the graphs do not close completely, which requires an approximation of the graph that is not good for all the data. SIMAD only allows us to determine the electrolyte resistance because the circuit used has a good response only at high frequencies, while at high frequencies, the values obtained for resistance were inconsistent. Due to the above, the authors decided to carry out the analysis of data obtained by the graphic method. Despite this, the data have been evaluated and considered qualitatively due to the complexity of the system.

Scanning electron microscopy

The effect of the *B. mojavensis* bacterium on 2024-T3 samples was observed by SEM. The results are shown in Figure 10. The alloy exposed to sterile EC (Figure 11a) showed a typical surface with corrosion products associated with the second phase. EDS analysis (Figure 11c) suggests an intermetallic phase chemical composition could be Al_2CuMg or Al_2Cu, since these are the predominant precipitating phases that occur in 2XXX alloys [31]. SEM images of alloy exposed to inoculated EC with bacteria *B. mojavensis* show a highly degraded surface with lost material (Figure 11b). EDS examination of the alloy corrosion product (Figure 10d) showed a copper-rich site probably associated with an accumulation of copper by local corrosion, due to the presence of precipitating phases rich in Cu [32].

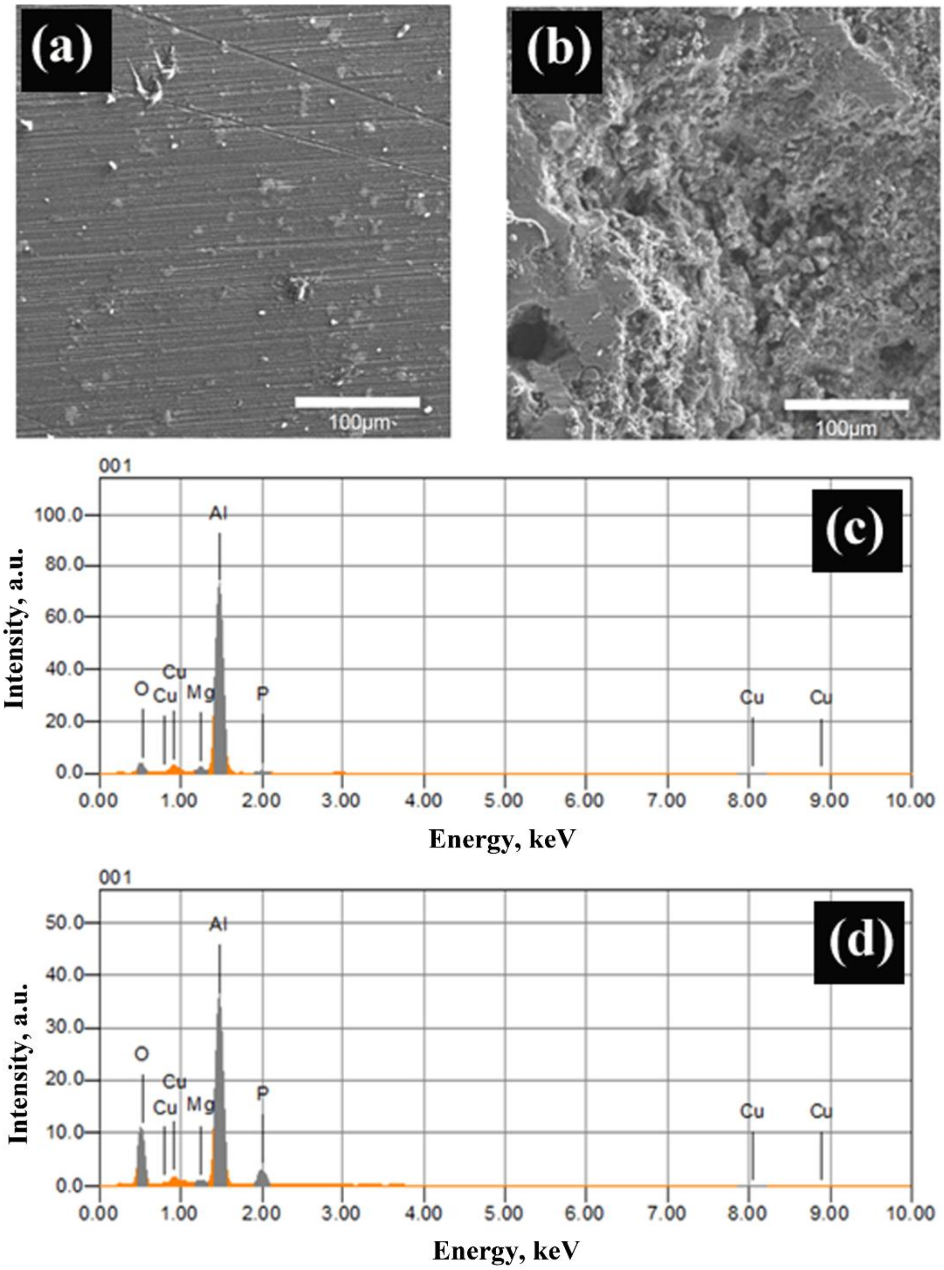

Figure 11. *SEM images of 2024-T3 exposed to (a) sterile and (b) inoculated electrolyte with B. mojavensis. Corresponding EDS (c) and (d)*

Conclusions

The present work evaluated the effect of the presence of second phases in the corrosion catalyzed by *B. mojavensis* bacteria. The electrochemical results showed the following important results:

1. Alloys with adequate heat treatment allowed to obtain surfaces with approximately ~67 % of the surface area corresponding to Al_2Cu type precipitates.

2. Alloys 2024-T3 showed accelerated corrosion when exposed to *B. mojavensis* bacteria.
3. Alloys designated ThT 05 showed a marked increase in impedance when exposed to *B. mojavensis* bacteria, suggesting a considerable slowing of corrosion.

The effect of the second phase in the corrosion and biocorrosion processes is crucial for understanding the phenomenon. The presence of Al_2Cu precipitates acts as cathode sites in aluminium alloys and is the cause of local and accelerated corrosion in these alloys in a chloride medium. The second phase could also affect the biocorrosion processes. However, using ~67 % on metal surfaces, the corrosive effect is masked by many precipitates, which does not allow adequate visualization of the bacteria in the corrosive process. Rather, a protective effect was observed, and the analysis was difficult using the techniques used. Detailed studies and methods such as XPS, are required to characterize the corrosion products.

Acknowledgements*: This work was supported by Agencia Nacional de Investigación y Dearrollo (ANID grants 11170419).*

References

[1] F. Ezzohra, E. Garchani, H. Lgaz, H. Lee, S.M. Ibrahim, M. Chafiq, Y. Gun, M. Rachid, Effects of heat treatment on the corrosion behavior and mechanical properties of aluminium alloy 2024, *Journal of Materials Research and Technology* **25** (2023) 1355-1363. https://doi.org/10.1016/j.jmrt.2023.05.278

[2] G. S. Chen, K.-C. Wan, M. Gao, R. P. Wei, T. H. Flournoy, Transition from pitting to fatigue crack growth—modeling of corrosion fatigue crack nucleation in a 2024-T3 aluminium alloy, *Materials Science and Engineering A* **219** (1996) 126-132. https://doi.org/10.1016/S0921-5093(96)10414-7

[3] B .J. Little, J. S. Lee, *Microbiologically Influenced Corrosion*, John Wiley & Sons Inc., Hoboken, New Jersey, USA, 2007. https://doi.org/10.1002/047011245X

[4] J. Yang, Y. Zhang, W. Chang, Y. Lou, H. Qian, Microbiologically influenced corrosion of FeCoNiCrMn high-entropy alloys by *Pseudomonas aeruginosa* biofilm, *Frontiers in Microbiology* **13** (2022) 1009310. https://doi.org/10.3389/fmicb.2022.1009310

[5] S. Sivasankaran, Aluminium Alloys - Recent Trends in Processing, Characterization, Mechanical Behavior and Applications, InTech Open, London, United Kingdom, 2017. https://doi.org/10.5772/68032

[6] J. Espinoza-Vergara, P. Molina, M. Walter, M. Gulppi, N. Vejar, F. Melo, M. Urzua, H. Muñoz, J. H. Zagal, X. Zhou, M. I. Azocar, M. A. Paez, Effect of pH on the Electrochemical Behavior of Hydrogen Peroxide in the Presence of *Pseudomonas aeruginosa*, *Frontiers in Bioengineering and Biotechnology* **9** (2021) 749057. https://doi.org/10.3389/fbioe.2021.749057

[7] S. Baeza, N. Vejar, M. Gulppi, M. Azocar, F. Melo, A. Monsalve, J. Pérez-Donoso, C.C. Vásquez, J. Pavez, J.H. Zagal, X. Zhou, G.E. Thompson, M. A. Páez, New evidence on the role of catalase in *Escherichia coli*–mediated biocorrosion, *Corrosion Science* **67** (2013) 32-41. https://doi.org/10.1016/j.corsci.2012.09.047

[8] L. Kuchariková, T. Liptáková, E. Tillová, D. Kajánek, E. Schmidová, Role of chemical composition in corrosion of aluminium alloys, *Metals (Basel)* **8** (2018) 581. https://doi.org/10.3390/met8080581

[9] L. M. Escobar, J. R. Rivera, E. Arbelaez, L. F. Torres, A. Villafañe, D. Díaz-Báez, I. Mora, G. I. Lafaurie, M. Tanaka, Comparison of Cell Viability and Chemical Composition of Six Latest Generation Orthodontic Wires, *International Journal of Biomaterials* **2021** (2021) 8885290. https://doi.org/10.1155/2021/8885290

[10] I. B. Beech, J. Sunner, Biocorrosion: Towards understanding interactions between biofilms and metals, *Current Opinion in Biotechnology* **15** (2004) 181-186. https://doi.org/10.1016/j.copbio.2004.05.001

[11] F. Mansfeld, The interaction of bacteria and metal surfaces, *Electrochimica Acta* **52** (2007) 7670-7680. https://doi.org/10.1016/j.electacta.2007.05.006

[12] B. M. Rosales, M. Iannuzzi, Aluminium AA2024 T351 aeronautical alloy. Part 1. Microbial influenced corrosion analysis, *Materials Science and Engineering A* **472** (2008) 15-25. https://doi.org/10.1016/j.msea.2007.06.079

[13] D. Hu, W. Lin, J. Zeng, P. Wu, M. Zhang, L. Guo, C. Ye, K. Wan, X. Yu, Profiling the microbial contamination in aviation fuel from an airport, *Biofouling* **35** (2019) 856-869. https://doi.org/10.1080/08927014.2019.1671977

[14] C. J. McNamara, T. D. Perry, R. Leard, K. Bearce, J. Dante, R. Mitchell, Corrosion of aluminium alloy 2024 by microorganisms isolated from aircraft fuel tanks, *Biofouling* **21** (2005) 257-265. https://doi.org/10.1080/08927010500389921

[15] R. Smith, *Biodeterioration and biodegradation*, Springer Dordrecht, Germany, 1991. ISBN 978-1-85166-626-3

[16] N. D. Vejar, J. Sacre, B. Collao, J. Perez-Donoso, M. A. Páez, F. Pineda, B. Worker, M. Sancy, Enhanced corrosion of 7075 alloy by the presence of *Bacillus megaterium*, *International Journal of Electrochemical Science* **11** (2016) 9723-9733. https://doi.org/10.20964/2016.11.33

[17] M. Sancy, A. Abarzúa, M.I. Azócar, J.M. Blamey, F. Boehmwald, G. Gómez, N. Vejar, M. Páez, Biofilm formation on aluminium alloy 2024: A laboratory study, *Journal of Electroanalytical Chemistry* **737** (2015) 212-217. https://doi.org/10.1016/j.jelechem.2014.08.015

[18] N. Vejar, S. Gutiérrez, N. Tareelap, C. Alvarado, R. Solís, C. Guerra, F. Pineda, M. Sancy, M. Páez, Influence of *Bacillus safensis* and *Bacillus pumilus* on the electrochemical behavior of 2024-T3 aluminium alloy, *Bioelectrochemistry* **143** (2022) 107950. https://doi.org/10.1016/j.bioelechem.2021.107950

[19] Q. Wang, G.M. Garrity, J.M. Tiedje, J.R. Cole, Naïve Bayesian classifier for rapid assignment of rRNA sequences into the new bacterial taxonomy, *Applied and Environmental Microbiology* **73** (2007) 5261-5267. https://doi.org/10.1128/AEM.00062-07

[20] C. Pillay, J. Lin, Metal corrosion by aerobic bacteria isolated from stimulated corrosion systems: Effects of additional nitrate sources, *International Biodeterioration & Biodegradation* **83** (2013) 158-165. https://doi.org/10.1016/j.ibiod.2013.05.013

[21] J. H. Kwon, P. Choi, S. Jo, H. Oh, K.Y. Cho, Y. K. Lee, S. Kim, K. S. Eom, Identification of electrode degradation by carbon corrosion in polymer electrolyte membrane fuel cells using the distribution of relaxation time analysis, *Electrochimica Acta* **414** (2022) 140219. https://doi.org/10.1016/j.electacta.2022.140219

[22] M. Kiran Kumar, C. Tyagi, A. Sahu, N. Desai, J. Manjhi, K. C. Mohan, Y. P. Reddy, S. K. Tiwari, L. K. Tomar, V. K. Sharma, Identification and Characterization of Staphylococcus aureus 16S rRNA gene isolated from different Food Specimens from South Indian Region, *Journal of Drug Delivery and Therapeutics* **10** (2020) 24-32. https://doi.org/10.22270/jddt.v10i5.4340

[23] A. Monsalve, L. Parra, D. Baeza, R. Solís, H. Palza, Mechanical properties and morphological characteristics of ARALL reinforced with TRGO doped epoxy resin, *Revista Matēria* **23** (2018) e-12228. https://doi.org/10.1590/s1517-707620180004.0562

[24] *ASM Handbook, Volume 4*, *Heat treating*, ASM International, Materials Park, Ohio, USA, 1991. ISBN 978 087 1703 798

[25] V. Nelson, J. Rojas, C. Alvarado G., R. Solís, F. Pineda, M. Sancy, L. Muñoz, M. Páez, Alumoxane film for corrosion protection of 2024 aluminium alloy, *Journal of Materials Research and Technology* **26** (2023) 4942-4956. https://doi.org/10.1016/j.jmrt.2023.08.192

[26] N. D. Vejar, J. Sacre, B. Collao, J. Perez-Donoso, M. A. Páez, F. Pineda, B. Worker, M. Sancy, Enhanced Corrosion of 7075 Alloy by the Presence of *Bacillus megaterium*, *International Journal of Electrochemical Science* **11** (2016) 9723-9733. https://doi.org/10.20964/2016.11.33

[27] R. Jia, D. Yang, D. Xu, T. Gu, Anaerobic Corrosion of 304 Stainless Steel Caused by the *Pseudomonas aeruginosa* Biofilm, *Frontiers in Microbiology* **8** (2017) 2335. https://doi.org/10.3389/fmicb.2017.02335

[28] D. Starosvetsky, J. Starosvetsky, R. Armon, Y. Ein-Eli, A peculiar cathodic process during iron and steel corrosion in sulfate reducing bacteria (SRB) media, *Corrosion Science* **52** (2010) 1536-1540. https://doi.org/10.1016/j.corsci.2010.01.013

[29] S. Sagadevan, S. Vennila, A.R. Marlinda, Y. Al-Douri, M. Rafie Johan, J. Anita Lett, Synthesis and evaluation of the structural, optical, and antibacterial properties of copper oxide nanoparticles, *Applied Physics A* **125** (2019) 489. https://doi.org/10.1007/s00339-019-2785-4

[30] C. You, M.A. Zabara, M.E. Orazem, B. Ulgut, Application of the Kramers-Kronig Relations to Multi-Sine Electrochemical Impedance Measurements, *Journal of The Electrochemical Society* **167** (2020) 020515. https://doi.org/10.1149/1945-7111/ab6824

[31] M.-L. de Bonfils-Lahovary, L. Laffont, C. Blanc, Characterization of intergranular corrosion defects in a 2024 T351 aluminium alloy, C*orrosion Science* **119** (2017) 60-67. https://doi.org/10.1016/j.corsci.2017.02.020

[32] E. Ghanbari, A. Saatchi, X. Lei, D.D. Macdonald, Studies on pitting corrosion of Al-Cu-Li alloys Part II: Breakdown potential and pit initiation, *Materials* **12** (2019) 1786. https://doi.org/10.3390/ma12111786